Journal of Electron Microscopy **57(6)**: 195–201 (2008)
doi: 10.1093/jmicro/dfn022

Physical: Letter

Rapid autotuning for crystalline specimens from an inline hologram

Andrew R. Lupini* and Stephen J. Pennycook

Materials Science and Technology Division, Oak Ridge National Laboratory, Oak Ridge, TN 37831, USA
*To whom correspondence should be addressed. E-mail: 9az@ornl.gov.

Abstract A method to measure the aberration function for a crystalline specimen from a single inline hologram or 'Ronchigram' by dividing it up into small patches is derived. Measurement of aberrations is demonstrated from both dynamical simulations and experimental Ronchigrams. This method should allow rapid fine-tuning on a variety of crystalline specimens and represents a key step toward active optics for scanning transmission electron microscopy.

Keywords STEM, aberration correction, Ronchigram, aberration measurement, Cs

Received 24 May 2008, accepted 7 October 2008, online 6 November 2008

Since the proof by Scherzer that the spherical (C_3) and chromatic (C_c) aberrations of round electron lenses are unavoidable [1] there have been considerable efforts to correct these aberrations using non-round elements, with notable recent successes [2,3]. Unfortunately, the measurement of aberrations, which forms an important part of aligning these non-round elements, is still many times slower than methods used in the related fields of active or adaptive optics [4]. The main aberration measurement algorithms presently used work poorly, if at all, for crystalline samples and instead require either a relatively amorphous region or a special tuning sample [5–8]. Most of these existing methods require multiple images, which can take a substantial time to acquire, imposing great demands on instrument stability. The ability to measure aberrations quickly at the same area used for imaging on crystalline samples would offer several potential benefits, including higher accuracy, less sensitivity to drift and perhaps the ability to monitor or dynamically correct aberrations during an image series.

The arrangement shown in Fig. 1 is essentially the configuration proposed by Gabor to overcome spherical aberration by forming an inline hologram [9]. An objective lens is used to focus a beam of electrons near the plane of a thin sample. The transmitted shadow image, also known as the Ronchigram [10], is often used to adjust a scanning transmission electron microscope (STEM) [11–15].

To give a concise description of the Ronchigram, we make the normal approximations (e.g. [16]) that after the probe has interacted with a thin sample Ψ , the transmitted wavefunction will be the product of the incident probe and a sample function. Thus, the intensity I recorded at the detector plane as a function of detection wavevector $\mathbf{K}_f$ and probe position $\mathbf{R}_0$ will be (the intensity of) the convolution of the aperture function and the diffraction pattern. Expressed mathematically, such a Ronchigram can be written as

$$I(\mathbf{K}_f, \mathbf{R}_0) = \iint \Psi(\mathbf{K}_i)\Psi^*(\mathbf{K}) \times e^{\frac{2\pi i}{\lambda}(\chi(\mathbf{K}_f-\mathbf{K}_i)-\chi(\mathbf{K}_f-\mathbf{K}))+2\pi i\mathbf{R}_0(\mathbf{K}-\mathbf{K}_i)} d\mathbf{K} d\mathbf{K}_i, \quad (1)$$

where λ is the wavelength, $\mathbf{K}$ and $\mathbf{K}_i$ are incident wavevectors and the aberration function χ is a function of angle, as given in reference [6].

We first model the Ronchigram of a crystalline material as having two delta-function diffraction spots at angles $\mathbf{g}$ and $\mathbf{h}$ with amplitudes a. Substituting this sample into (1), performing the integral and neglecting constant terms, gives the intensity in the overlap region as

$$I(\mathbf{K}_f, \mathbf{R}_0) = 2a^2 \cos(2\pi(\lambda^{-1}\chi(\mathbf{K}_f - \mathbf{h}) - \lambda^{-1}\chi(\mathbf{K}_f - \mathbf{g}) + \mathbf{R}_0.(\mathbf{g} - \mathbf{h}))). \quad (2)$$

The resulting sinusoidal fringes depend on the aberrations, which may be inferred from the fringe spacings [11, 17–23].

Adding more diffracted beams will give additional interference effects. To reduce the notation we ignore the phase change from the sample, which depends on factors such as thickness (reference [11] used *ia*, which changes the cosine to a sine), and probe position. Setting the on-axis beam intensity to unity gives the three-beam pattern as

$$\begin{aligned} I(\mathbf{K}_f, \mathbf{R}_0) = {} & 2a\cos(2\pi\lambda^{-1}(\chi(\mathbf{K}_f) - \chi(\mathbf{K}_f - \mathbf{g}))) \\ & + 2a\cos(2\pi\lambda^{-1}(\chi(\mathbf{K}_f - \mathbf{h}) - \chi(\mathbf{K}_f))) \\ & + 2a^2\cos(2\pi\lambda^{-1}(\chi(\mathbf{K}_f - \mathbf{h}) - \chi(\mathbf{K}_f - \mathbf{g}))). \end{aligned} \quad (3)$$

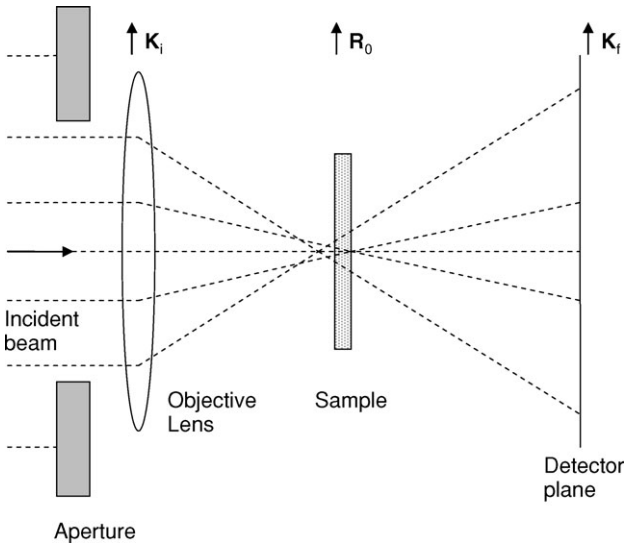

Fig. 1. A simplified schematic of the formation of an electron Ronchigram. An incident beam (left) is focused near to the sample (center) and the shadow image recorded in the far field (right).

Rearranging this equation and neglecting the weaker terms in a^2, which is a good approximation in a thin crystal, gives

$$I(\mathbf{K}_f, \mathbf{R}_0) = 4a\cos(\pi\lambda^{-1}(\chi(\mathbf{K}_f - \mathbf{h}) - \chi(\mathbf{K}_f - \mathbf{g}))) \times \cos(\pi\lambda^{-1}(2\chi(\mathbf{K}_f) - \chi(\mathbf{K}_f - \mathbf{g}) - \chi(\mathbf{K}_f - \mathbf{h}))). \quad (4)$$

The expressions for multiple beams follow in a similar way. We conclude that the three-beam case is essentially the two-beam result (a discrete first difference) modulated by an additional term (a discrete second difference). This extra term, shown by Lin and Cowley [11], can make the fringes vanish; however, the fringes rarely cancel completely over a large area and then the focus can be changed slightly to avoid this condition.

Fourier transforms are often used to measure fringe spacings, since a constant spacing gives two delta functions. Boothroyd has demonstrated that the Fourier transform of the Ronchigram can be used to provide quantitative information about the aberrations [18]. However, the difficulty is that the spacings change across the Ronchigram. We therefore consider a *small patch* of the Ronchigram at a particular detection angle $\mathbf{T}$, such that $\mathbf{K}_f = \mathbf{T} + \mathbf{K_T}$ for small $\mathbf{K_T}$, and Taylor series expand:

$$\chi\left(\mathbf{K}_f - \mathbf{h}\right) - \chi\left(\mathbf{K}_f - \mathbf{g}\right) \approx \chi\left(\mathbf{T} - \mathbf{h}\right) - \chi\left(\mathbf{T} - \mathbf{g}\right) + \mathbf{K_T}.\nabla\left(\chi\left(\mathbf{T} - \mathbf{h}\right) - \chi\left(\mathbf{T} - \mathbf{g}\right)\right) + \ldots. \quad (5)$$

Thus, the condition for a 'small' patch is that it is reasonable to neglect terms of order $\mathbf{K_T^2}$ and higher. This expansion allows us to Fourier transform Eq. (2) over $\mathbf{K_T}$, giving the coordinates of the delta functions as

$$\mathbf{S_T} = \pm\nabla\left(\chi\left(\mathbf{T} - \mathbf{g}\right) - \chi\left(\mathbf{T} - \mathbf{h}\right)\right), \quad (6)$$

where $\mathbf{S_T}$ is the coordinate of the delta-function 'spot' in the patch at $\mathbf{T}$. As the fringe spacings normally vary slightly over the patch, the spots are not perfect delta functions. For spherical aberration, the Fourier transforms of large patches will resemble 'comets' (reference [18] and Fig. 2). In that case, we consider the head of the comet, which fails when there is not a single clear maximum.

Equation (6) reveals that the Fourier transform of a small patch from a Ronchigram will resemble a diffraction pattern from the same area, but the spot positions will depend on the local derivatives of the aberration function as well as the reciprocal lattice (**g**-vectors). This result is remarkable because it provides a route to measure aberrations from a single crystalline Ronchigram. We Fourier transform a series of N small patches at different angles ($\mathbf{T}_1 \ldots \mathbf{T}_N$) and measure the position of the spots ($\mathbf{S_T}_1 \ldots \mathbf{S_T}_N$). Equation (6) then relates the measured spot coordinates to their respective **g**-vectors and the derivatives of the aberration function, meaning that a simple least-squares routine can be used to fit an aberration function. The problem will be over-determined if more than two spots are used and a full solution will not be possible if all the **g**-vectors are collinear.

To make the fit a linear problem, we assumed that the **g**-vectors were known, which is straightforward for known samples; however, this equation also provides a method to determine the **g**-vectors, even when the sample and defocus are both unknown. We measure a spot position as $\mathbf{S1_T}$, change focus by a calibrated step dC_1 and measure the position of the same spot again as $\mathbf{S2_T}$, to give

$$\mathbf{g} = \left(\mathbf{S2_T} - \mathbf{S1_T}\right)/dC_1. \quad (7)$$

Put simply, the initial and final positions of the spots will depend on all of the aberrations, but a pure focus change will cause a spot to move along its **g**-vector. Because the sign of the focus change is known, this method also allows us to determine the sign of defocus and thus avoid the sign ambiguity in Eq. (6).

As multiple beam interference was neglected, we now consider the three-beam result in more detail. Fourier transforming Eq. (3) suggests that there will be additional spots at

$$\mathbf{S_T} = \pm\nabla\left(\chi\left(\mathbf{T} - \mathbf{h}\right) - \chi\left(\mathbf{T}\right)\right) \text{ and } \mathbf{S_T} = \pm\nabla\left(\chi\left(\mathbf{T} - \mathbf{g}\right) - \chi\left(\mathbf{T}\right)\right). \quad (8)$$

However, fitting to Eq. (8) did not work well in practice, probably because we could not separate the $\{+\mathbf{g}, 0\}$ and the $\{0, -\mathbf{g}\}$ terms. If $\mathbf{h} = -\mathbf{g}$, these two terms are equivalent apart from a shift of origin [18] and can cancel out. As the two sets of fringes are translated by **g**, the intensity of the Fourier transform will be modulated by $\cos(2\pi\mathbf{S}.\mathbf{g})$, which gives the 'interference fringes' in Fig. 2. This interference makes the spot locations harder to determine and provides a source of errors for the present work. When higher order aberrations are significant, these interference fringes can be analyzed to determine the **g**-vectors (as in [21]).

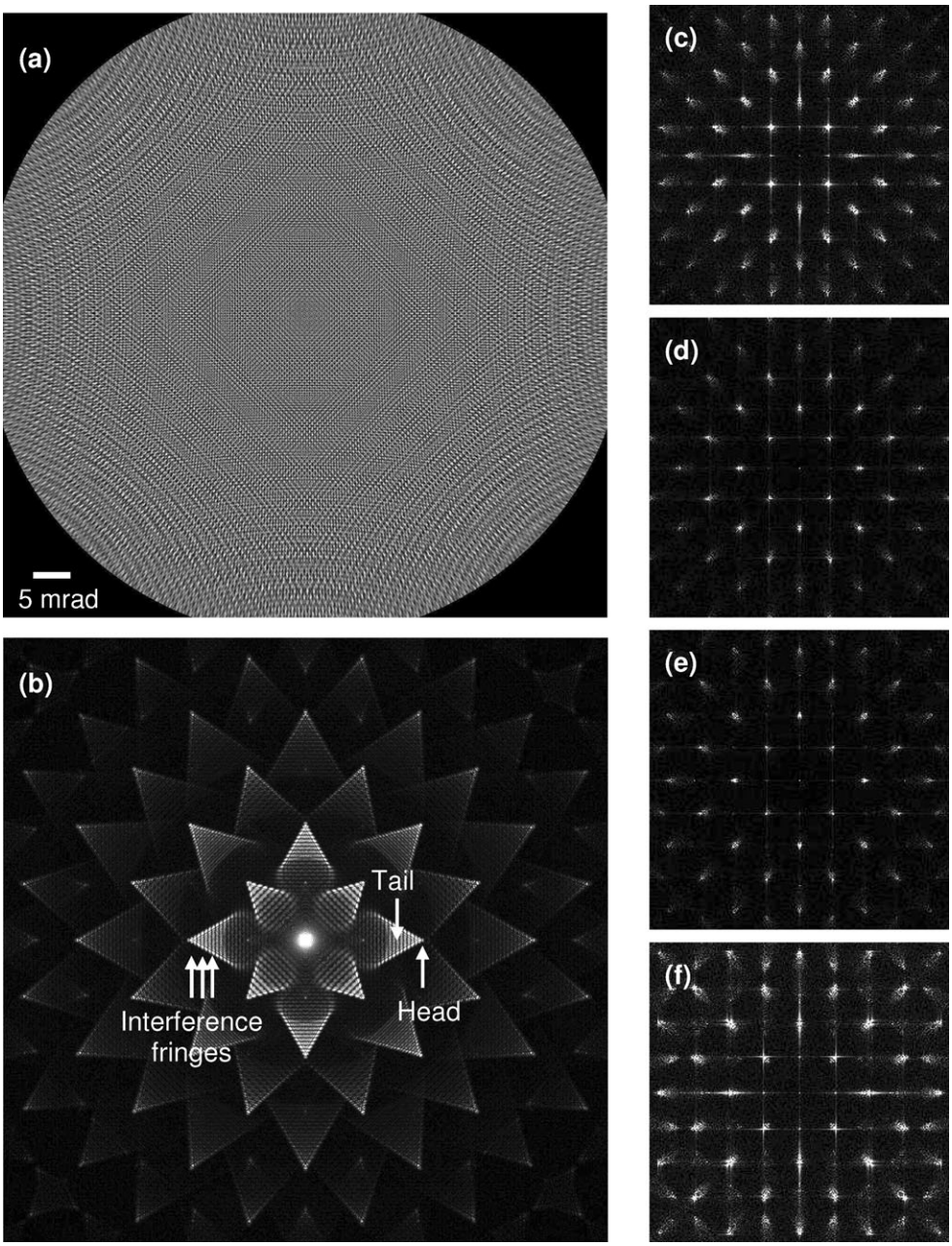

Fig. 2. (a) Ronchigram simulation of 4-nm-thick $SrTiO_3$ [100]. Defocus = −600 nm, C_3 = 0.1 mm at 300 kV. (b) The Fourier transforms of a large patch from (a). (c–f) The Fourier transform of small patches from the same simulation at (c) −600, (d) −650, (e) −700 and (f) −750 nm defocus. The spots are in slightly different positions in each frame.

Instead we consider the Fourier transform of Eq. (4), where the product of the two cosine functions will give a convolution between their Fourier transforms. The first term will give delta functions at

$$\mathbf{S_T} = \pm\nabla\left(\chi\left(\mathbf{T}-\mathbf{h}\right) - \chi\left(\mathbf{T}-\mathbf{g}\right)\right)/2. \qquad (9)$$

These spots will be convolved with the transform of the (more slowly varying) second term, which we neglect. In this work, we fit directly to Eq. (9) including arbitrary numbers of spots. For historical reasons, we first tried to approximate these equations by the second derivatives of the aberration function, which was found to give a good fit, but introduces errors from the higher-order aberrations (see the supplementary data online).

As an initial test of the accuracy of our proposed method, we performed simulations of Ronchigrams using the code provided by Kirkland [24] and analyzed them. An example Ronchigram of $SrTiO_3$ viewed down the [100] direction is shown in Fig. 2, for a thickness of 4 nm, defocus of −600 nm and C_3 of 0.1 mm, with other aberrations zero. A script was used to extract small patches from the simulated images and Fourier transform them. The spots were located by automatically seeking local maxima near initial estimates for the spot positions. These estimates are automatically generated and

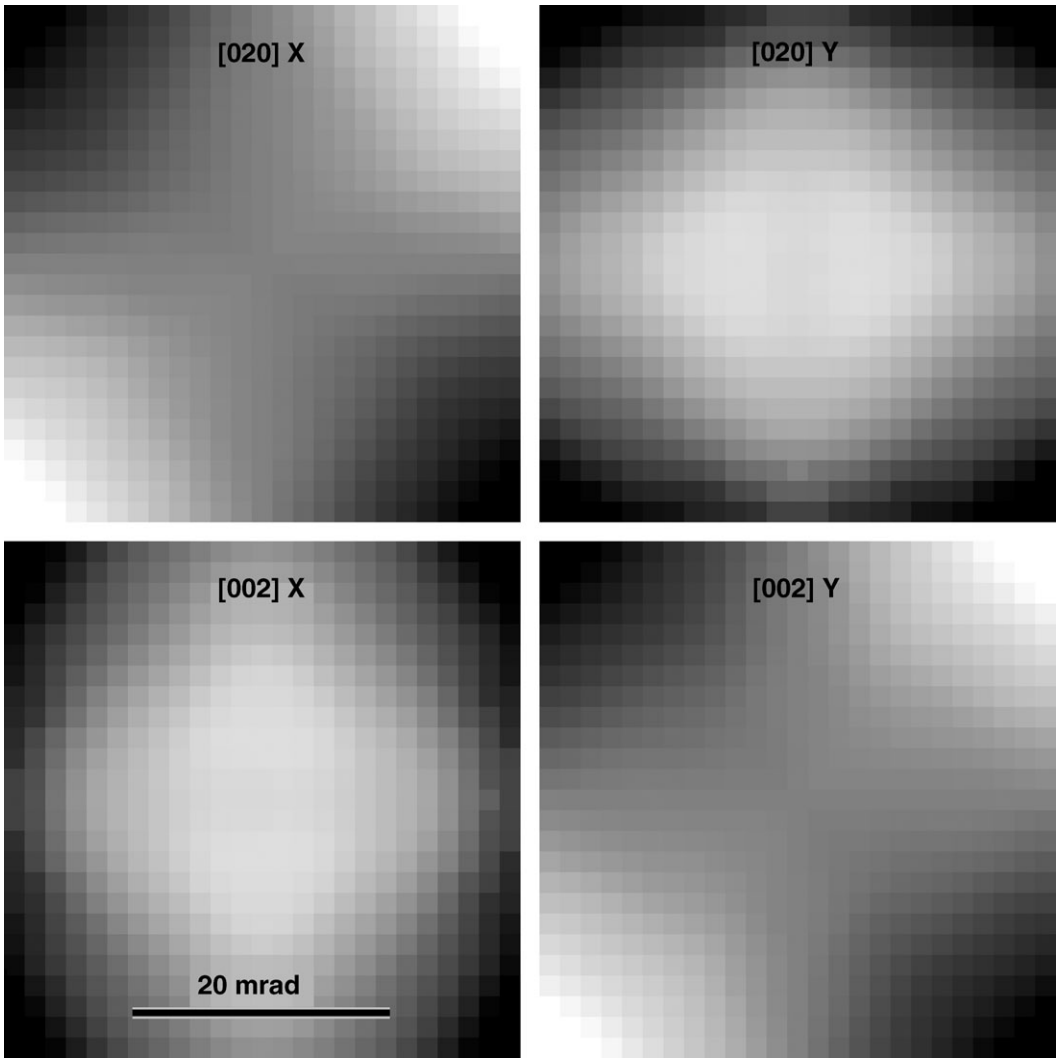

Fig. 3. Graphical representations of the spot coordinates measured from the simulation in Fig. 2 using 25 × 25 patches. The intensity of each pixel represents the shift of the spot in the patch at that angle in the *X* and *Y* directions of the [020]- and [002]-type spots, respectively. Each intensity scale goes from −4 (black) to +4 (white) pixels. These plots closely resemble the second derivatives of the aberration function (see the supplementary data online).

then approved by the user, who can control which spots are chosen. The spot coordinates measured for this example are illustrated in Fig. 3, which uses shades of gray to indicate changes in the spot positions. We treated the sample as 'unknown' and used a defocus series of four frames separated by −50-nm steps to probe the errors. The fitted aberrations are summarized in Table 1 for two different thicknesses and choices of different spots. The measured defocus was within ~3 nm of the known values, −600 to −750 nm. The C_3 was measured as ~0.085 mm in the single worst measurement, but was normally within a few percent of the known value. Most other aberrations were measured comparatively well.

We repeated simulations for various combinations of first-, second- and third-order aberrations. Table 2 summarizes another example measurement under similar conditions, with 20 nm of 2-fold astigmatism and 1000 nm of

Table 1. Aberration coefficients in nm (average ± standard deviation) measured using four spots (020, 002, 011, 01-1) for the four-frame focal series (defocus −600, −650, −700, −750 nm), simulated with $C_3 = 0.1$ mm, other aberrations zero

Thickness	Focus offset	Astigmatism	Three-fold	Coma	C_3
0.5 nm	+2.5 ± 0.07	0.1 ± 0.06	3.3 ± 2.4	8.1 ± 3.4	98 920 ± 177
4 nm	+2.7 ± 0.9	0.2 ± 0.01	2.1 ± 1.3	2.6 ± 0.6	86 966 ± 1957

Analysis used 5 × 5 patches, each ~16 mrad diameter, spaced by ~6.3 mrad.

Table 2. Aberration coefficients in nm (average ± standard deviation) measured for a four-frame focal series (defocus −600, −650, −700, −750 nm) simulated with 20-nm astigmatism and 1000-nm 3-fold astigmatism; coma and C_3 were zero

Thickness	Focus offset	Astigmatism	Three-fold	Coma	C_3
0.5 nm	+1.7 ± 0.4	20.5 ± 0.1	1000 ± 11.9	10.2 ± 4.3	645 ± 988
4 nm	+7.0 ± 0.5	20.6 ± 0.03	949 ± 5.1	23.2 ± 21.6	−1600 ± 1245

Analysis used the same conditions as in Table 1.

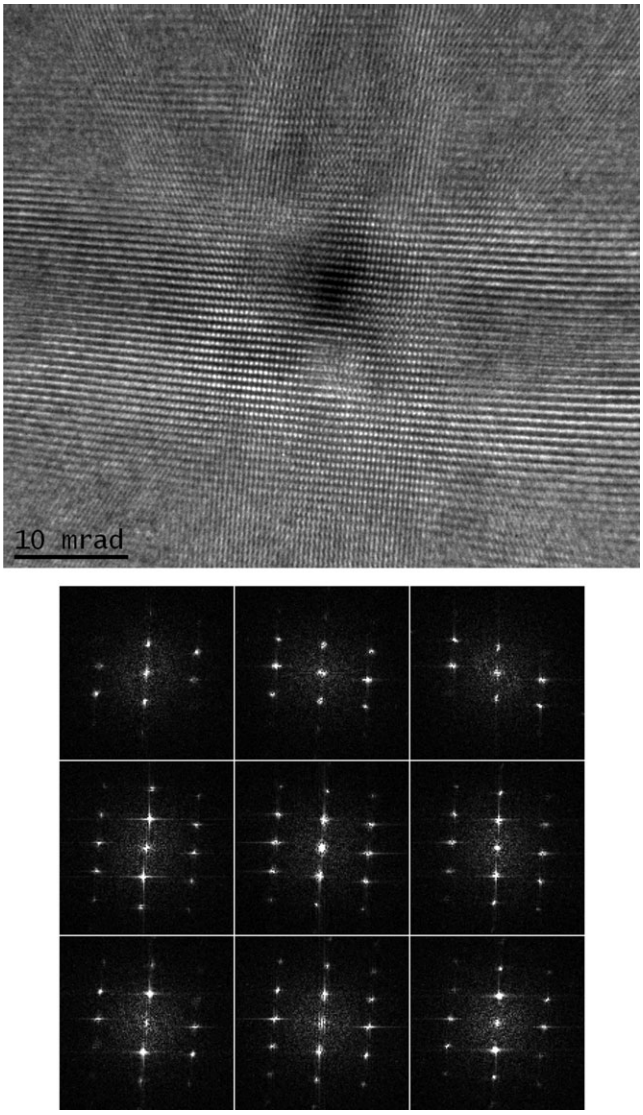

Fig. 4. (Top) Representative extract from a focal series of Ronchigrams from Si [112]. (Bottom) The Fourier transforms of 3 × 3 patches (each enlarged by two and cropped to show only the central area) cut from the corresponding positions from the Ronchigram. Each patch was 15 mrad across, spaced by 15 mrad.

3-fold astigmatism. Again the measured aberrations matched the simulated values well. The direction of the 2-fold astigmatism was correct to ∼2° and that of the 3-fold to better than 1°. The absolute error in the measurement was larger than the standard deviation, which is partly caused by the small (∼2%) error in measuring the **g**-vectors. This error in the **g**-vectors gave a systematic contribution to the overall errors, but is interesting because it reveals that such methods may be sensitive to any lattice distortions of more than a few pm. Further simulations indicated that sample thicknesses up to 20 nm could be used. At large thicknesses, the spots became more diffuse, which gave a dependence of the accuracy on the sample thickness that could be investigated in future.

To further test our method, we used experimental data from several aberration-corrected instruments. A script was used to acquire Ronchigrams at regular focus intervals and measure the aberrations. We used the known lattice spacing d to provide the calibration of the focus steps. If the only significant aberration is defocus C_1, for a spot radius S, we find that

$$C_1 = Sd. \tag{10}$$

Equation (10) also provides a fast method to measure chromatic aberration (by changing accelerating voltage), which will be important for C_c-corrected instruments. The relativistically corrected value of C_c for the VG Microscope's HB603U was measured as 1.6 mm and the measured value for the FEI Titan 80-300 also agreed well with the value provided by the manufacturer. The largest uncertainty was the accuracy of the camera length calibrations.

Figure 4 shows an example Si [112] Ronchigram taken on the FEI Titan 80-300 with the CEOS aberration corrector running. Following the change from the tuning sample to the Si sample, we expected to find astigmatism and coma. In this example, the astigmatism was measured as ∼5 nm with a standard deviation of <1 nm over the focus range used (∼400–550-nm defocus); see Table 3. The 3-fold astigmatism and coma were measured as a few hundred nm, with standard deviations of the order of tens of nm. The C_3 had been zeroed using the CEOS software and so it is not completely clear if the measurement of a few μm is real or just reflects the accuracy of the measurement under the conditions used. We found a dependence of the measured aberrations on patch size, which suggests that there may still be some residual errors. For patches with fewer pixels, the uncertainty due to the finite pixel size was significant. For larger patches, the random errors were smaller, although the multiple-beam interference effects were more visible in the transforms, which could contribute to systematic errors. The accuracy could be improved by optimizing the camera length or using a higher quality camera with more pixels. Despite the approximations made, the standard deviations are of a similar order to those obtained with

Table 3. Aberration coefficients in nm (average ± standard deviation) measured from 10 frames, using four spots, from an experimental focal series with patches spaced by 3 mrad

Patch pixels	Focus step	Astigmatism	Three-fold	Coma	C_3
128 × 128	13.9 ± 1.1	4.3 ± 1.3	141 ± 29	434 ± 79	−15 942 ± 5329
256 × 256	14.1 ± 1.0	4.5 ± 0.3	137 ± 20	543 ± 46	−9636 ± 2867

For 256 pixels, the analysis used 9 × 9 patches, each with ∼15 mrad diameter; and for 128 pixels, 7 × 7 patches were used, each with ∼7.5 mrad diameter.

current versions of either the CEOS [5] or the Nion [6] software packages. The magnitudes of the measured aberrations were consistent with these established methods, although the acquisition time was substantially faster. We anticipate that further developments in the implementation, such as an improved spot-locating algorithm, will produce more accurate measurements in future.

In conclusion, we have demonstrated a method to measure the aberration function from the electron Ronchigram of a crystalline specimen. The advantage over previous methods is that it can use unknown, crystalline samples and faster acquisition times. When the sample and defocus are both unknown, two Ronchigrams are needed but once the vectors describing the sample have been measured, this method can measure the aberration function from a single Ronchigram. Another potential use is to dynamically monitor aberrations after each frame in a depth series [25], with very little overhead, since the Ronchigram acquisition time of 0.1–0.5 s, is 10–100 times faster than a typical STEM image. The similarity of the description in Eq. (1) to a lateral shearing interferometer suggests that this method might be applicable to other fields, for example as a lens test [10] in light optics.

Acknowledgements

The research was supported by the Division of Materials Science and Engineering of the U.S. Department of Energy. Some of the instrumentation used in this research was provided as part of the TEAM project, funded by the Department of Energy, Office of Science. Critical comments from several colleagues, including Drs. Nellist, Krivanek, Ramasse and Kenik, and the reviewers are gratefully acknowledged.

Supplementary data

Supplementary data are available online at http://jmicro.oxfordjournals.org/.

References

1 Scherzer O (1936) Über einige Fehler von Elektronenlinsen. *Zeit. Phys*. **101**: 593–603.

2 Nellist P D, Chisholm M F , Dellby N, Krivanek O L, Murfitt M F, Szilagyi Z S, Lupini A R, Borisevich A, Sides W H, Jr., and Pennycook S J (2004) Direct Sub-Angstrom Imaging of a Crystal Lattice. *Science* **305**: 1741.

3 Haider M, Uhlemann S, Schwan E, Rose H, Kabius B, and Urban K (1998) Electron microscopy image enhanced. *Nature* **392**: 768–769.

4 Roddier F (ed.) (1999) *Adaptive Optics for Astronomy* (Cambridge University Press, Cambridge).

5 Haider M, Rose H, Uhlemann S, Kabius B, and Urban K (1998) Towards 0.1 nm resolution with the first spherically corrected Transmission Electron Microscope. *J. Electron Microsc.* **47**: 395–405.

6 Krivanek O L, Dellby N, and Lupini A R (1999) Towards sub-Å electron beams. *Ultramicroscopy* **78**: 1–11.

7 Dellby N, Krivanek O L, Nellist P D, Batson P E, and Lupini A R (2001) Progress in aberration-corrected scanning transmission electron microscopy. *J. Electron Microsc.* **50**: 177–185.

8 Zemlin F, Weiss K, Schiske P, Kunath W, and Herrmann K H (1978) Coma-free alignment of high resolution electron microscopes with the aid of optical diffractograms. *Ultramicroscopy* **3**: 49–60.

9 Gabor D (1948) A new microscopic principle. *Nature* **161**: 777–778.

10 Ronchi V (1964) Forty years of history of a grating interferometer. *Appl. Opt.* **3.2**: 437–451.

11 Lin J A and Cowley J M (1986) Calibration of the operating parameters for an HB5 STEM instrument. *Ultramicroscopy* **19**: 31–42.

12 Wang S-Y and Cowley J M (1995) Shadow Images for In-Line Holography in a STEM instrument. *Microsc. Res. Tech.* **30**: 181–192.

13 Cowley J M (1979) Adjustment of a STEM instrument by use of shadow images. *Ultramicroscopy* **4**: 413–418.

14 James E M and Browning N D (1999) Practical aspects of atomic resolution imaging and spectroscopy in STEM. *Ultramicroscopy* **78**: 125–139.

15 Rodenburg J M and Macack E B (2002) Optimizing the resolution of TEM/STEM with the Electron Ronchigram. *Microsc. Anal.* **90**: 5–7.

16 Rodenburg J M and Bates R H T (1992) The theory of super-resolution electron microscopy via Wigner-distribution deconvolution. *Phil. Trans. R. Soc. A* **339**: 521–553.

17 Ramasse Q and Bleloch A L (2005) Diagnosis of aberrations from crystalline samples in scanning transmission electron microscopy. *Ultramicroscopy* **106**: 37–56.

18 Boothroyd C B (1997) Quantification of Energy Filtered Lattice Images and Coherent Convergent Beam Patterns. *Scan. Microsc.* **11**: 31–42.

19 Mitsuishi K, Takeguchi M, Kondo Y, Hosokawa F, Okamoto K, Sannomiya T, Hori M, Iwama T, Kawazoe M, and Furuya K (2006) Ultrahigh-Vacuum Third-Order Spherical Aberration (Cs) Corrector for a Scanning Transmission Electron Microscope. *Microsc. Microanal.* **12**: 456–460.

20 Yamazaki T, Kotaka Y, Kikuchi Y, and Watanabe K (2005) Precise measurement of third-order spherical aberration using low-order zone-axis Ronchigrams. *Ultramicroscopy* **106**: 153–163.

21 Kuramochi K, Yamazaki T, Kotaka Y, Kikuchi Y, Hashimoto I, and Watanabe K (2008) Measurement of twofold astigmatism of probe-forming lens using low-order zone-axis ronchigram. *Ultramicroscopy* **108**: 339–345.

22 Spence J C H and Zuo J M (1992) *Electron Microdiffraction* (Plenum, New York and London).

23 Spence J C H (1996) Quantitative electron microdiffraction. *J. Electron Microsc.* **45**: 19–26.

24 Kirkland E J (1998) *Advanced Computing in Electron Microscopy* (Plenum, New York and London).

25 Borisevich A Y, Lupini A R, and Pennycook S J (2006) Depth sectioning with the aberration-corrected scanning transmission electron microscope. *Proc. Natl Acad. Sci. USA* **103**: 3044–3048.